# Growth mechanism and electronic properties of stacking mismatch boundaries in wurtzite III-nitride material

Hang Zang,[1] Zhiming Shi,[1] Jianwei Ben,[1] Ke Jiang,[1] Yang Chen,[1] Shanli Zhang,[1] Mingrui Liu,[1] Tong Wu,[1] Yuping Jia,[1] Xiaojuan Sun,[1,*] and Dabing Li[1,2,†]

[1]*State Key Laboratory of Luminescence and Applications, Changchun Institute of Optics, Fine Mechanics and Physics, Chinese Academy of Sciences, Changchun 130033, China*

[2]*Center of Materials Science and Optoelectronics Engineering, University of Chinese Academy of Sciences, Beijing 100049, China*

(Received 17 June 2022; accepted 12 April 2023; published 24 April 2023)

III-nitride materials including AlN, GaN, and InN are promising for semiconductor industry applications; however, the material growth process gives rise to high defect densities in the epilayer, which can affect the device performance. A systemical understanding of the defect physics is necessary for realistic applications. Among the defects in III-nitride materials, the stacking mismatch boundary (SMB) is a kind of extended defect generated due to the presence of a stacking fault, whose structure-function relationship is still not well understood. Here, we report on a first-principles investigation of the growth and electronic properties of the SMB in III-nitride materials. Based on the wurtzite crystal symmetry, it is found that the SMBs can be categorized into three basic types, depending on the terrace edge of the coalescent normal and stacking-fault regions on the (0001) surface, and the corresponding edge type is controllable by varying the chemical potential and initial nucleation size during the material growth process. Additionally, it is revealed that SMBs produce in-gap states in III-nitride materials with various properties, including itinerant magnetism with high Curie temperature and optical transition correlated with the experimentally observed sub-band-gap spectrum. It is worth noting that one type of SMB is a possible source of the yellow luminescence that is widely observed in GaN. Our findings add comprehensive insight into the SMB in III-nitride materials; the unique growth controllable property of an SMB is also a possible routine to broaden the applications of III-nitride materials.

DOI: 10.1103/PhysRevB.107.165308

## I. INTRODUCTION

Defects play crucial roles in devices based on solid material since their electronic properties are completely different from those of perfect crystals. For the III-nitride materials, which are widely used in electronic and optoelectronic devices [1–8], the film usually contains a high density of defects since they are mainly obtained by heteroepitaxy. The extended defects including dislocation and stacking fault in III-nitride materials usually cause current leakage and nonradiative carrier recombination [7,8], which degrades the device performance to a large extent. Various techniques including x-ray diffraction (XRD) [9,10] and high-resolution transmission electron microscopy (HRTEM) [11–13] have been used to measure the extended defects in III-nitride materials. For the characterization of stacking faults, the XRD technique, as a convenient nondestructive approach, can give an overall estimation of the defect-induced lattice distortion in III-nitride materials. HRTEM is a more appropriate technique for probing stacking faults since it can directly measure the local atomic structure of a post-processed wafer, and corresponding studies have been performed in AlN [11], GaN [12], and InN [13].

From an atomic point of view, stacking faults in wurtzite (WZ) III-nitride materials are the local structures with zinc-blende (ZB) coordination [14,15]. The WZ phase is more stable than the ZB phase, but their energy difference is small [16,17] and the ZB phase can be generated during the material growth process [11–13]. The boundary between the ZB and WZ phases along the [0001] direction forms the basal-plane stacking fault (BSF), where the local structures are still tetrahedrally coordinated, and it has been reported that there is a band offset between WZ and ZB regions perpendicular to the BSF direction [18,19]. A more complex case is the boundary between ZB and WZ phases within the (0001) surface, where wrong bonds are formed: Such a line defect is referred to as a stacking mismatch boundary (SMB) or a double positioning boundary (DPB) [20–23].

Many investigations have been carried out to study the SMB in III-nitride materials. In early studies, the SMB with $sp^2$-bonded configurations were theoretically proposed [24,25] and later observed by HRTEM at the surface of InGaN/GaN multiple quantum well structures [26–28]; similar defect structures were observed in III-V nanowires [29]. It was also found that the SMB could exhibit a more compact structure at the AlN/SiC [21] and GaN/SiC interfaces [22,23] and within the III-nitride alloy epilayers [30,31]. Additionally, the SMB along the (11-20) surface with 4|8 structures have been proposed [32–34] and observed in recent scanning transmission electron microscope (STEM) measurements in

*sunxj@ciomp.ac.cn
†lidb@ciomp.ac.cn

 ©2023 American Physical Society

GaN [35]. In these studies, different atomic structures of the SMB were identified, but a comprehensive view of how the structure is generated during material growth is still lacking, and it is not clear how the electronic property of the SMB is directly related to its atomic structure.

In this paper, we present first-principles investigations of the generation mechanism of the SMB based on the crystal growth theory. It is found that, depending on the edge of the coalescent WZ/ZB terrace on the (0001) surface, SMBs in III-nitride materials can be classified into three categories that are determined by the edge type of coalescent WZ and ZB terraces. The electronic structure results show that the SMB generates in-gap states, which lead to various magnetic and optical properties. The correlation with experimental observation and possible application on the base of the unique property of the SMB are discussed.

## II. METHODS

All first-principles calculations are performed based on density functional theory (DFT) [36,37] methods implemented in the PWmat [38,39] package. The ONCV-PWM pseudopotential [40] with an energy cutoff of 60 Ry is adopted, where Al ($3s^23p^1$), Ga ($4s^24p^1$), In ($5s^25p^1$), and N ($2s^22p^3$) are treated as valence electrons. The Perdew-Burke-Ernzerhof (PBE) [41] and the Heyd-Scuseria-Ernzerhof (HSE06) [42,43] functionals are employed. The mixing value of Hartree-Fock exchange is set to be 0.30, 0.18, 0.15 for the slab model of AlN, GaN, InN to reproduce the experimental band gap. The DFT-D3 dispersion interaction [44] is employed to deal with the van der Waals interaction. The spin-polarization effect is considered in all the calculations. A k-mesh interpolation $<0.05 \times 2\pi/\text{Å}$ is adopted for all calculations. The atomic positions are optimized until the maximum force on each atom is $<0.02$ eV/Å. The calculated lattice parameters for III-nitride materials are listed in Table S1 in the Supplemental Material [45].

The absorption spectrum is calculated with the random phase approximation (RPA), which is based on Fermi's golden rule:

$$\epsilon_2(\omega) = \sum_{i\in \mathrm{VB},\, j\in \mathrm{CB}} |\langle\psi_i|\frac{\partial H}{\partial k}|\psi_j\rangle|^2 \delta(E_j - E_i - \omega). \quad (1)$$

Here, $\partial H/\partial k$ is the momentum operator, $E_i$ is the eigenenergy of the state $\psi_i$. The transition dipole moment is defined as

$$\mu_{ij} = \frac{\langle\psi_i|p|\psi_j\rangle}{E_i - E_j}. \quad (2)$$

The radiative lifetime between state $i$ and $j$ is obtained based on Fermi's golden rule [46,47]:

$$W_{\mathrm{rad}}(\omega_{ij}) = \frac{\omega_{ij}^3 n|\langle\psi_i|e\cdot r|\psi_j\rangle|^2}{3\pi\epsilon_0\hbar c^3} = \frac{4\alpha}{3}\frac{\omega_{ij} n|\langle\psi_i|p|\psi_j\rangle|^2}{m_e^2 c^2}, \quad (3)$$

where $\omega_{ij}$ is the frequency of a photon, $n$ is the refractive index, $\epsilon_0$ is the vacuum permittivity, $\hbar$ is the reduced Planck constant, $c$ is the vacuum speed of light, $m_e$ is the mass of an electron, and $\alpha = \frac{e^2}{4\pi\epsilon_0 c\hbar}$ is the fine structure constant. Here, for AlN, we use $n = 2.3$ at the transition energy of 4.6 eV and $n = 2.6$ at the transition energy $>5.9$ eV; for GaN, we use $n = 2.4$ for the transition energy of 2.2 eV and $n = 2.7$ at the transition energy $>3.3$ eV [48].

## III. RESULTS AND DISCUSSION

The growth property of the monoatomic-height WZ and ZB terraces on the (0001) surface of III-nitride materials is investigated first. As shown in Fig. 1(a), WZ/ZB terraces on the (0001) surface can exhibit different shapes depending on the exposed edge. Take the case of AlN as an example: The terrace on the (0001) surface has zigzag (Z) and armchair (A) edges, the lack of inversion symmetry results in two types of Z edges including $Z_{\mathrm{Al}}$ and $Z_{\mathrm{N}}$ with Al and N atoms as the termination. The reconstructed edge of $K_{\mathrm{N}}$ ($K_{\mathrm{Al}}$) is formed by attaching an Al (N) atom to $Z_{\mathrm{N}}$ ($Z_{\mathrm{Al}}$), and the reconstructed edge of $A_{\mathrm{Al}}$ ($A_{\mathrm{N}}$) is formed by attaching an Al (N) atom to A. The detailed edge structures are shown in Fig. S1 in the Supplemental Material [45].

During the material growth process, the two-dimensional terrace shape on the surface is determined by the relative terrace edge energy under the equilibrium growth condition [49–52]. Here, the terrace edge energy is calculated with a slab model (see Fig. S2 in the Supplemental Material [45]). For the case of AlN, the edge energy is defined as

$$\gamma_{\mathrm{edge}} = \frac{E_{\mathrm{tot}} - E_{\mathrm{slab}} - x\mu_{\mathrm{Al}} - y\mu_{\mathrm{N}}}{L}, \quad (4)$$

where $E_{\mathrm{tot}}$ is the total energy of a bare slab with the terrace on the (0001) surface, $E_{\mathrm{slab}}$ is the energy of a bare slab, $\mu_{\mathrm{Al}}$ and $\mu_{\mathrm{N}}$ represent the chemical potentials of Al and N, $x$ and $y$ represent the number of Al and N atoms in the terrace, and $L$ represents the length of the edge. The calculations are at the PBE level [41]. At the thermodynamic equilibrium condition, the chemical potentials satisfy $\mu_{\mathrm{Al}} + \mu_{\mathrm{N}} = \mu_{\mathrm{AlN}}^0$ where $\mu_{\mathrm{AlN}}^0 = -327.74$ eV is the calculated energy of a pair of AlN in bulk AlN. The reference chemical potential of $\mu_{\mathrm{Al}}$ is obtained at the condition where the Al and N species arrive on the (0001) surface with equal quantity [51], which results in $\mu_{\mathrm{Al}} = -57.19$ eV.

The calculated edge energies for the WZ terrace as a function of $\mu_{\mathrm{Al}}$ are shown in Fig. 1(b). The edge energies show a linear dependence on $\mu_{\mathrm{Al}}$ and different types of edges can be stable at certain ranges of $\mu_{\mathrm{Al}}$. The reconstructed edges of $A_{\mathrm{Al}}/A_{\mathrm{N}}$, $K_{\mathrm{N}}$, and $K_{\mathrm{Al}}$ have a larger slope than A, $Z_{\mathrm{Al}}$, and $Z_{\mathrm{N}}$, indicating the dangling atoms contribute to the edge energy to a large extent. Notably, the $Z_{\mathrm{N}}$ edge is the stablest one in a wide range of $\mu_{\mathrm{Al}}$, and several types of edges have close edge energy around $\mu_{\mathrm{Al}} = -57.19$ eV. The edge energies of the ZB terrace are like the WZ terrace, as indicated by the small energy difference compared with the absolute edge energy shown in Fig. 1(c).

The Wulff diagram represents the natural shape of the terrace, which is of importance to determine the type of exposed edge of the coalescent WZ/ZB terrace during the SMB generation process. The two-dimensional Wulff structure of the terrace is obtained based on the edge energy [53]; as shown in Fig. 1(d), it exhibits truncated polygon features formed from hexagon (formed by A, $A_{\mathrm{Al}}$, and $A_{\mathrm{N}}$) and triangle (formed by $Z_{\mathrm{Al}}$, $Z_{\mathrm{N}}$, $K_{\mathrm{Al}}$, and $K_{\mathrm{N}}$) shapes. The WZ and ZB terraces exhibit

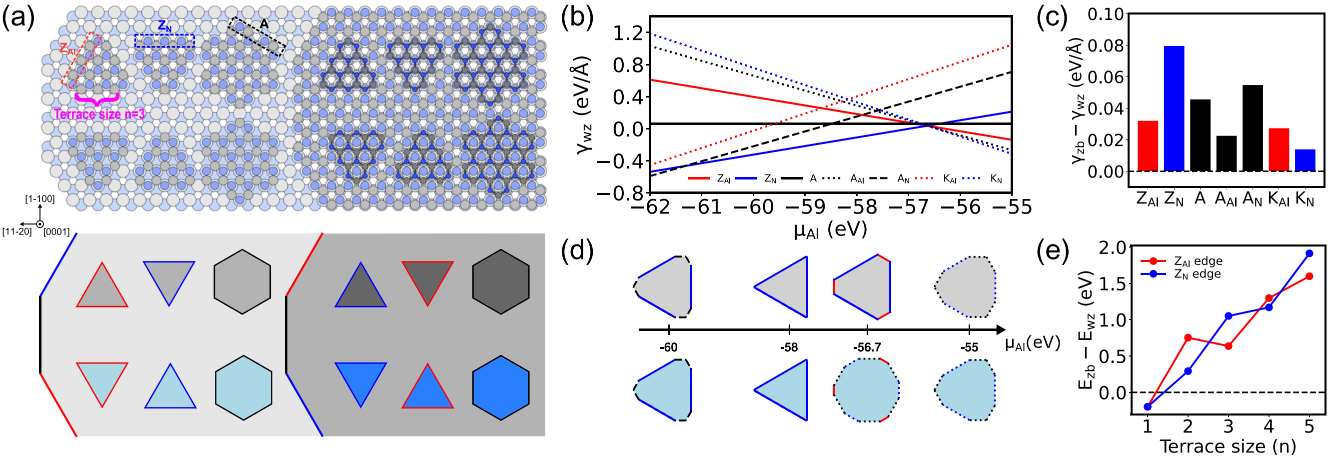

FIG. 1. (a) Atomic structures of wurtzite (WZ) and zinc-blende (ZB) terraces on the (0001) surface of AlN with different heights of steps; the gray and blue balls represent Al and N atoms. The schematic representations of the terrace edges and step edges are shown at the bottom; the WZ and ZB terraces are filled with gray and blue colors, respectively. The darker colors and smaller atoms indicate the higher step height. (b) Edge energies of WZ terrace on AlN (0001) surface as a function of $\mu_{\mathrm{Al}}$. (c) Edge energy difference between ZB and WZ terraces on AlN (0001) surface. (d) Wulff structures of WZ and ZB terraces on AlN (0001) surface at different $\mu_{\mathrm{Al}}$; different types of edges are represented by lines in (b); WZ and ZB terraces are filled with gray and blue colors. (e) Total energy difference between ZB and WZ terraces on AlN (0001) surface with different sizes.

similar Wulff shapes except at the chemical potentials around $\mu_{\mathrm{Al}} = -57.19$ eV. Since different types of edge energies are close around this point, a small difference between WZ and ZB edge energy causes a large difference in the relative edge energy and therefore a large difference of Wulff shape. Notably, all the principle edge directions can occur for both WZ and ZB terraces at the same $\mu_{\mathrm{Al}}$. Additionally, the occurrence condition of WZ and ZB terraces on the (0001) surface of AlN is assessed. As shown in Fig. 1(e), the relative stability between WZ and ZB terraces altered when the size of the terrace increased, and the ZB phase is more stable at the smallest terrace size. Since the terrace strongly interacts with the surface, the coordination property is maintained as that of the initial terrace during the following terrace expansion growth mode; therefore, the WZ/ZB coordination is controllable via the initial nucleation size on the (0001) surface. The properties for surface terraces in GaN and InN are shown in Figs. S4 and S5 in the Supplemental Material [45]; they exhibit qualitative similarities to the case of AlN.

Due to the intrinsic WZ symmetry of III-nitride materials, there exists an orientation relationship between WZ/ZB terraces during the step flow growth. Figure 1(a) shows a schematic shape and orientation of the WZ and ZB terraces with ideal edges on different atomic step layers. For terraces with the same kind of Z edges on the same atomic step, the triangle direction is reversed between the WZ and ZB terraces. For terraces with the same kind of Z edges on neighboring atomic steps, the triangle direction is reversed between the same WZ (ZB) terraces. For terraces with the A edge, the hexagon direction is always the same regardless of the WZ/ZB coordination or the step height. Also, during the step-flow growth of the WZ structure, the type of Z edges are altered for neighboring steps.

Experimentally, anisotropy of step-flow growth and triangular islands have been observed on the (0001) surface of III-nitride materials at different growth conditions [54–59]. Also, a double step bunching of GaN has been observed [54,58]. Based on our previous analysis, the occurrence of the Z edge of the terrace should be responsible for these observations since there exists a certain chemical potential for the triangle Wulff structure, and the neighbor steps process altered types of $Z_{\mathrm{Al,Ga,In}}$ and $Z_{\mathrm{N}}$ edges which have different edge energies in a certain growth condition. Additionally, Shi *et al.* [60] found the initial stage nucleation kinetics plays a primary role in determining the WZ/ZB structure of GaN by studying the occurrence of triangle islands with inversed direction, whereas the WZ and ZB phases could be formed at different initial nucleation temperatures. Our previous results for the relative stability of different sized terraces should be a reason for such a phenomenon.

Based on the WZ/ZB terrace property on the (0001) surface, the SMB can be classified into three types, as shown in Fig. 2. These structures are consistent with those observed experimentally, as we have introduced before. The structure of SMB1 has been observed at the surface of InGaN/GaN multiple quantum well structures [26–28]. The structure of SMB2 has been observed at AlN/SiC [21] and GaN/SiC [22,23] interfaces. The structure of SMB3 has been observed in heteroepitaxial GaN [35].

For the case of AlN, the generation of SMB1, SMB2, and SMB3 begins from the coalescent of WZ and ZB terraces with $Z_{\mathrm{Al}}/K_{\mathrm{Al}}$, $Z_{\mathrm{N}}/K_{\mathrm{N}}$, and $A/A_{\mathrm{Al}}/A_{\mathrm{N}}$ edges, respectively. Since the stacking fault, i.e., the local ZB phase, is a low-energy defect in III-nitride materials [16,17], the SMB is expected to extend for only short distances in the [0001] direction before it is terminated [24]. Here, we consider the SMB with the shortest case. A schematic four-step layer-by-layer growth process of SMB is proposed, as shown in Fig. S6 in the Supplemental Material [45]. In the first step, a coexistence of WZ and ZB terraces on the (0001) surface occurs, and a smooth boundary can be formed between WZ and ZB terraces since their edge energies are similar at the same chemical potential. In the

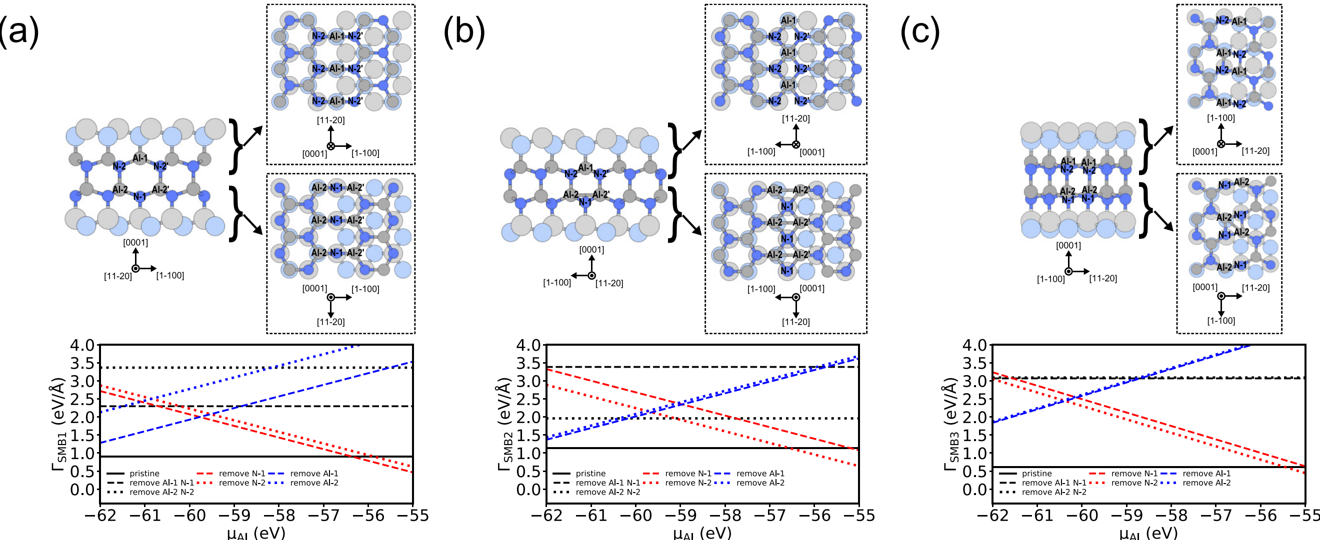


FIG. 2. Atomic structures and formation energies as a function of $\mu_{\mathrm{Al}}$ for (a) SMB1, (b) SMB2, and (c) SMB3, and their reconstructed structures in AlN.

second step, the formation of pure WZ terraces at the second layer occurs. This can be achieved by adopting a normal WZ phase growth condition. At this layer, WZ terraces show different orientations on different sides of the boundary, which is caused by the ZB phase inclusion in the lower layer. In the third step, a normal WZ nucleation process on top of one side of the boundary occurs, followed by an expansion process across the boundary. At this layer, the WZ/ZB coordination is reversed when crossing the boundary, and the WZ and ZB terraces have the same orientation. In the fourth step, the normal growth process of the WZ phase occurs.

To assess the stability and local structure of SMB, for the case of AlN, we calculate the formation energy of the pristine SMB with the least number of nonfourfold-coordinated atoms and its variants with local atoms removed, as marked in Fig. 2. The formation energy is defined as

$$\Gamma_{\mathrm{SMB}} = \frac{E_{\mathrm{tot}} - x\mu_{\mathrm{Al}} - y\mu_{\mathrm{N}}}{L}, \tag{5}$$

where $E_{\mathrm{tot}}$ represents the total energy of the system, $x$ and $y$ represent the number of Al and N atoms, and $L$ represents the length of the SMB. The chemical potentials satisfy $\mu_{\mathrm{Al}} + \mu_{\mathrm{N}} = \mu^{0}_{\mathrm{AlN}}$. The atomic model is shown in Fig. S3 in the Supplemental Material [45].

The calculated formation energies for the three types of SMB with different structures are shown in Fig. 2. The pristine SMB is stable in a wide range of chemical potentials. The formation energies for SMB1, SMB2, and SMB3 are 0.90, 1.14, and 0.61 eV/Å, respectively. SMBs with Al or N atoms removed can be stable at certain N- or Al-rich conditions. It should be noted that, though SMB3 has the lowest formation energy, the formation of SMB1 and SMB2 is still possible since the generation of the SMB depends on the coalescent terrace determined by growth history. The formation energy of SMBs in GaN and InN are listed in Figs. S7 and S8 in the Supplemental Material [45]. They are like the case of the SMB in AlN except that the pristine form of SMB2 in InN can only be stable in a narrow chemical potential range, which may result in structural instability during the growth process.

To further investigate the electronic property of the SMB in III-nitride materials, we calculate the energy band with PBE [41] and HSE06 [42] functionals. A slab supercell model that contains only one type of SMB is used. The surface metal and nitrogen atoms are passivated with pseudohydrogen with $1.25e$ and $0.75e$ charges, respectively. Here, we consider the pristine SMB with the least number of nonfourfold-coordinate atoms. The results are shown in Fig. 3, and the defect bands near the Fermi level are marked as $\alpha$ and $\beta$. For SMB1 and SMB2, $x$, $y$, and $z$ correspond to the [11-20], [0001], and [1-100] directions, respectively. For SMB3, $x$, $y$, and $z$ correspond to the [0001], [1-100], and [11-20] directions, respectively. For SMB1 and SMB2, the $x$ direction is along the direction of the SMB, while for SMB3, the $y$ direction is along the direction of the SMB. The corresponding K path is defined on the base of $x$, $y$, and $z$.

The unit cells for modeling the property of an individual SMB in III-nitride materials are shown in Fig. 3(a). They are like the ones used in previous theoretical works regarding the dislocation band structures of CdTe, GaAs compounds, etc. [61,62]. For a benchmark of the cell size, we have calculated the band structures using the same model shown in Fig. 3(a) with different lattice parameters along the directions perpendicular to the SMB. The results are shown in Figs. S9–S11 in the Supplemental Material [45]. For the benchmark tests with different lattice parameters, we observe similar band gap values and band dispersions, as shown in Fig. 3, indicating the current model is suitable for the band structure calculation. The lattice parameters of all the unit cells for modeling the SMB are listed in Table S2 in the Supplemental Material [45], and the corresponding defect density, which is defined by counting the number of defect lines in a unit area perpendicular to it, is included.

The PBE and HSE06 band structures are qualitatively similar. After introducing the Hartree-Fock exchange interaction, the experimental band gap can be well reproduced for the

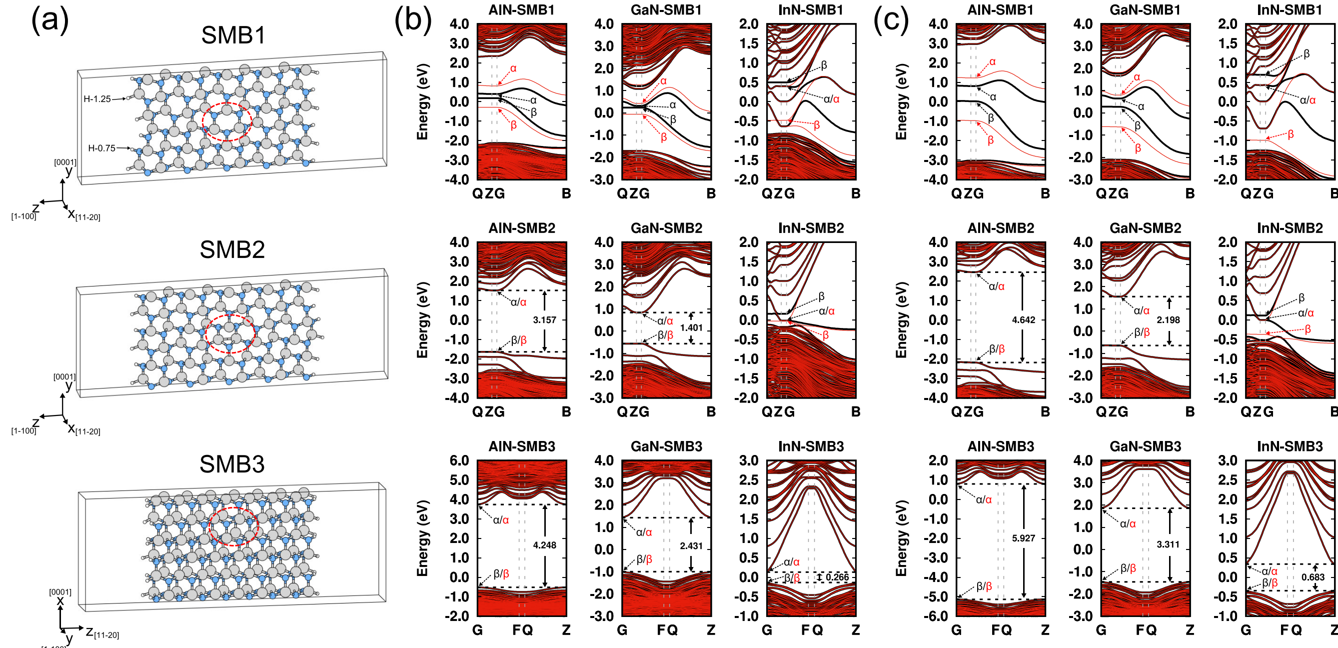


FIG. 3. (a) Atomic structures for different types of stacking mismatch boundary (SMB) in AlN. (b) PBE and (c) HSE06 band structures for SMB; the black and red lines correspond to the spin-up and spin-down channels. Here, $G$ (0.0, 0.0, 0.0), $F$ (0.0, 0.5, 0.0), $Q$ (0.0, 0.5, 0.5), $Z$ (0.0, 0.0, 0.5), and $B$ (0.5, 0.0, 0.0) refer to the high-symmetry special points in the first Brillouin zone; the Fermi level is set to zero.

bulk model (see Fig. S12 in the Supplemental Material [45]). Additionally, the defect bands are moved toward the band edge since they are mainly contributed by the cation and anion bonds. For SMB1 in AlN and GaN, the defect bands of $\alpha$ and $\beta$ are located within the band gap, and they are both spin polarized. The defect bands cross the Fermi level in one spin channel. For SMB1 and SMB2 in InN, the defect bands $\alpha$ locate within the conduction bands in both spin channels, while the defect bands $\beta$ exhibit a spin polarization. An inversed sequence of the $\alpha$ and $\beta$ states occurs in different spin channels. For SMB2 in AlN and GaN, the defect bands $\alpha$ and $\beta$ are spin unpolarized, and they generate a direct band gap of $\sim$4.6 and 2.2 eV, respectively. For SMB3 in AlN, GaN, and InN, spin-unpolarized $\alpha$ and $\beta$ states are generated within the band gap, and the band gaps are close to the bulk phase. The corresponding wave function profiles for the defect states are shown in Fig. S13 in the Supplemental Material [45]. The wave function profiles are distributed along the SMB which are correlated well with the large band dispersion along this direction.

The origin of the magnetism of the SMB can be understood by the Stoner mechanism [63], as the one-dimensional character of the defect state of the SMB gives rise to van Hove singularities at the upper and lower energy parts of the density of states. Additionally, the large dispersion of the defect energy bands indicates the itinerant character of electrons. For the case of SMB1 in AlN and GaN, the defect band edges for the $\alpha$ and $\beta$ states are close, and a large density of both occupied and unoccupied states occurs around the Fermi surface, which causes a magnetic instability around the Fermi surface. Both the $\alpha$ and $\beta$ states exhibit a spin splitting. For the case of SMB1 and SMB2 in InN, the defect states of $\alpha$ and $\beta$ mix with the conduction bands, which again results in a large density of occupied and unoccupied states around the Fermi surface; however, the $\alpha$ state exhibits a delocalized rather than a one-dimension property, as indicated by the wave function profiles. Only the $\beta$ states exhibit a spin splitting. The corresponding spin densities are shown in Fig. S14 in the Supplemental Material [45], and it is well correlated with the wave functions of the defect states. To further test the magnetism property induced by the SMB, we have estimated the Curie temperature with the mean-field approach [64]. By varying the temperature factor in the Fermi-Dirac distribution $f(E) = 1/[\exp(\frac{E-E_f}{k_B T}) + 1]$, the total magnetic moment is obtained at the PBE level. As shown in Fig. 4(a), the total magnitude (sum of the absolute magnetic moment on each atom) of the system completely changes to zero above the critical temperature, which indicates that the magnetism should come from the itinerant electron.

For SMB2 in AlN and GaN as well as SMB3 in AlN, GaN, and InN, though the defect state exhibits a one-dimensional character, the high density of states around the Fermi surface is fully occupied, which does not lead to a magnetic instability around the Fermi surface. Additionally, we have calculated the magnetic property of the SMB by using carrier doping, which produces both occupied and unoccupied states around the Fermi surface. As shown in Fig. 4(b), it is found that, for the case of SMB2 in AlN, under the hole doping (positive carrier density) or electron doping (negative carrier density), the magnetic property can both be achieved when the carrier concentration is above a certain value. The spin densities at a certain carrier density are shown in Fig. S15 in the Supplemental Material [45]. However, it is noted that a carrier density $\sim 10^{19}$ cm$^{-3}$ is needed to obtain the magnetism, which is a high carrier concentration for III-nitride materials [7,65].

Another important effect of the SMB in III-nitride materials is the optical property that can be directly measured. We

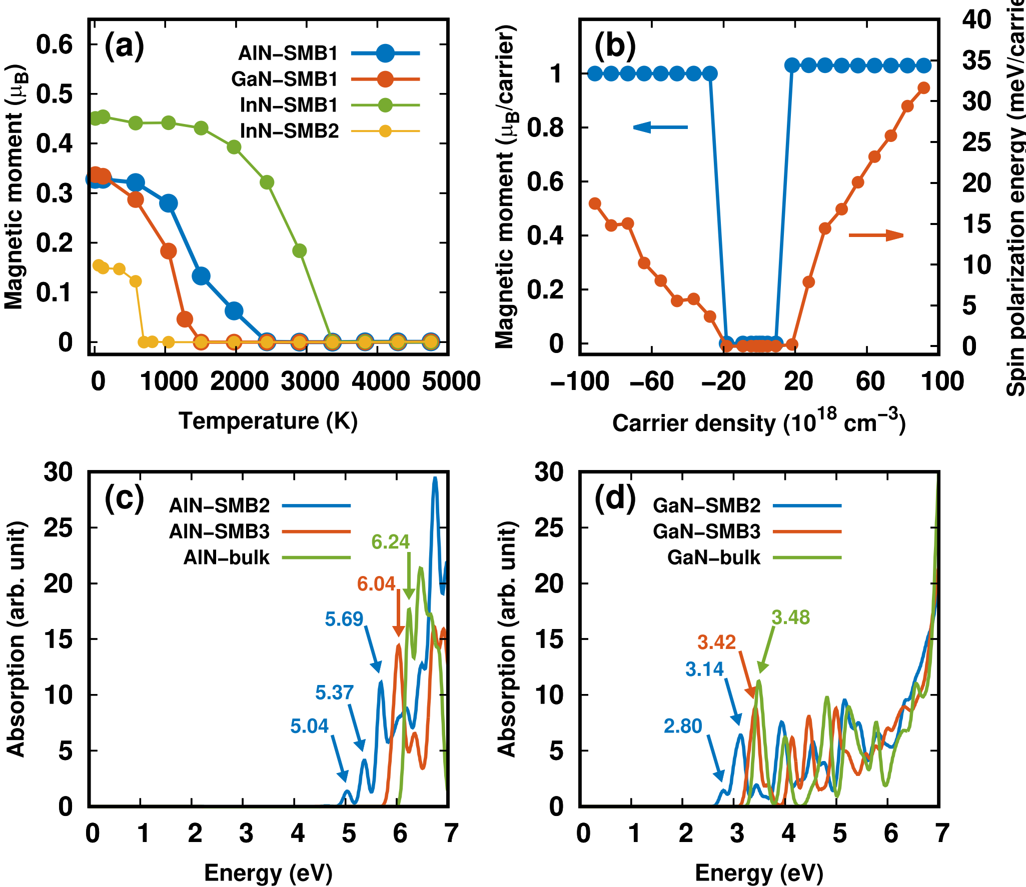


FIG. 4. (a) Temperature dependence of the total magnetic moment of AlN-SMB1, GaN-SMB1, InN-SMB1, and InN-SMB2. (b) Carrier density dependence of the total magnetic moment and spin-polarization energy of AlN-SMB2 at a $k_BT = 0.001$ eV (11.6 K) condition. Absorption spectrums for stacking mismatch boundaries (SMBs) in (c) AlN and (d) GaN.

have calculated the absorption spectra of SMB2 and SMB3 in wide band-gap AlN and GaN with the random phase approximation method at the HSE06 level. The results are shown in Figs. 4(c) and 4(d). Experimentally, various defect-induced optical peaks have been observed in wide band-gap AlN in the range of 4.6–6.2 eV [66–69] and GaN in the range of 2.2–3.4 eV [70–79]. The calculated optically allowed absorption peaks should be possible sources for the sub-band-gap absorptions. We have also estimated the radiative property of the SMB-induced defect state based on Fermi's golden rule [46,47]. The results are listed in Table I. The radiative transition rate between defect states of SMB3 is at the same magnitude as the transition between the valence band maximum (VBM) and the conduction band minimum (CBM) in perfect material. The radiative transition between defect states of SMB2 is much slower. The calculated radiative lifetimes are 141.0 ns and 36.9 μs between $\beta$ and $\alpha$ for AlN and GaN, respectively. It is noted that a decay time of the 2.2 eV yellow luminescence varying from nanosecond to millisecond time scale had been observed in undoped GaN [71]. Our results,

TABLE I. Transition dipole moment $|\mu_{ij}|^2$ (in units of a.u.), transition energy $\Delta E_{ij}$ (in units of eV), and radiative rate $W(\omega_{ij})$ (in units of $\text{ns}^{-1}$) at the $G$ (0.0, 0.0, 0.0) point calculated with the HSE06 functional.

| | State | AlN | | | GaN | | |
|---|---|---|---|---|---|---|---|
| | | $\|\mu_{ij}\|^2$ | $\Delta E_{ij}$ | $W(\omega_{ij})$ | $\|\mu_{ij}\|^2$ | $\Delta E_{ij}$ | $W(\omega_{ij})$ |
| SMB2 | $\beta \leftrightarrow \alpha$ | 0.029 | 4.642 | $7.09 \times 10^{-3}$ | 0.001 | 2.198 | $2.71 \times 10^{-5}$ |
| | $\beta - 1 \leftrightarrow \alpha$ | 0.640 | 5.045 | — | 6.867 | 2.797 | — |
| | $\beta - 2 \leftrightarrow \alpha$ | 1.349 | 5.363 | — | 17.310 | 3.031 | — |
| | $\beta - 3 \leftrightarrow \alpha$ | 4.551 | 5.687 | — | 25.400 | 3.162 | — |
| SMB3 | $\beta \leftrightarrow \alpha$ | 2.914 | 5.927 | 1.68 | 18.600 | 3.311 | 1.94 |
| Bulk | VBM $\leftrightarrow$ CBM | 8.407 | 6.238 | 5.64 | 25.490 | 3.448 | 3.00 |

therefore, indicate the SMB2 in GaN might be a possible source of it.

## IV. CONCLUSIONS

In summary, we have systemically investigated the SMB in III-nitride material based on DFT calculation. The growth property of terraces on the (0001) surface reveals that the WZ/ZB coordination of the terrace can be controlled by initial nucleation size, and the edge type of terrace can be controlled by the chemical potential. Based on the symmetry of the WZ structure, three types of SMBs are classified, and it is found that the SMB with the least number of nonfourfold-coordinated atoms is stable in a wide chemical potential range. The energy band structure calculation shows that the SMB generates in-gap states with a one-dimensional character. The optical transitions between defect states are responsible for experimentally observed sub-band-gap spectra. Specifically, it is found that SMB2 in GaN generates a band gap of 2.2 eV, with a radiative lifetime on the microsecond scale, which might be one of the origins of the yellow luminescence widely observed in GaN. Additionally, itinerant magnetism is confirmed for the SMB in III-nitride materials at both intrinsic and carrier doping conditions, which comes from the Fermi surface instability induced by the one-dimensional density of the state character of the SMB. The magnetic property of certain types of SMBs in III-nitride materials can realize metal and semiconductor features in different spin channels. As the fabrication of devices based on III-nitride materials is compatible with the complementary metal-oxide-semiconductor technique, it is possible to realize energy-efficient large-scale integrations of these functionalities of the SMB.

## ACKNOWLEDGMENTS

This paper was supported by the National Natural Science Foundation of China (Grants No. 62121005, No. 12004378, No. 12234018, No. 61834008, and No. 61827813), the Key Research Program of Frontier Sciences, Chinese Academy of Sciences (CAS; Grant No. ZDBS-LY-JSC026), and the Youth Innovation Promotion Association of CAS (Grant No. 2023223).


[1] I. Akasaki and H. Amano, Jpn. J. Appl. Phys. **36**, 5393 (1997).
[2] S. Nakamura, Science **281**, 956 (1998).
[3] S. Strite and H. Morkoç, J. Vac. Sci. Technol. B **10**, 1237 (1992).
[4] F. A. Ponce and D. P. Bour, Nature (London) **386**, 351 (1997).
[5] O. Ambacher, J. Phys. D: Appl. Phys. **31**, 2653 (1998).
[6] S. C. Jain, M. Willander, J. Narayan, and R. V. Overstraeten, J. Appl. Phys. **87**, 965 (2000).
[7] D. Li, K. Jiang, X. Sun, and C. Guo, Adv. Opt. Photon. **10**, 43 (2018).
[8] M. Kneissl, T.-Y. Seong, J. Han, and H. Amano, Nat. Photonics **13**, 233 (2019).
[9] S. R. Lee, A. M. West, A. A. Allerman, K. E. Waldrip, D. M. Follstaedt, P. P. Provencio, D. D. Koleske, and C. R. Abernathy, Appl. Phys. Lett. **86**, 241904 (2005).
[10] M. A. Moram and M. E. Vickers, Rep. Prog. Phys. **72**, 036502 (2009).
[11] K. Dovidenko, S. Oktyabrsky, and J. Narayan, J. Appl. Phys. **82**, 4296 (1997).
[12] D. N. Zakharov, Z. Liliental-Weber, B. Wagner, Z. J. Reitmeier, E. A. Preble, and R. F. Davis, Phys. Rev. B **71**, 235334 (2005).
[13] S. Strite, D. Chandrasekhar, D. J. Smith, J. Sariel, H. Chen, N. Teraguchi, and H. Morkoç, J. Cryst. Growth **127**, 204 (1993).
[14] C.-Y. Yeh, Z. W. Lu, S. Froyen, and A. Zunger, Phys. Rev. B **46**, 10086 (1992).
[15] G. M. Dalpian and S.-H. Wei, Phys. Rev. Lett. **93**, 216401 (2004).
[16] A. F. Wright, J. Appl. Phys. **82**, 5259 (1997).
[17] C. Stampfl and C. G. Van de Walle, Phys. Rev. B **57**, R15052 (1998).
[18] Z. Z. Bandić, T. C. McGill, and Z. Ikonić, Phys. Rev. B **56**, 3564 (1997).
[19] A. Belabbes, L. C. de Carvalho, A. Schleife, and F. Bechstedt, Phys. Rev. B **84**, 125108 (2011).
[20] Z. Sitar, M. J. Paisley, B. Yan, and R. F. Davis, Mater. Res. Soc. Symp. Proc. **162**, 537 (1989).
[21] S. Tanaka, R. S. Kern, and R. F. Davis, Appl. Phys. Lett. **66**, 37 (1995).
[22] D. J. Smith, D. Chandrasekhar, B. Sverdlov, A. Botchkarev, A. Salvador, and H. Morkoç, Appl. Phys. Lett. **67**, 1830 (1995).
[23] B. N. Sverdlov, G. A. Martin, H. Morkoç, and D. J. Smith, Appl. Phys. Lett. **67**, 2063 (1995).
[24] J. E. Northrup, J. Neugebauer, and L. T. Romano, Phys. Rev. Lett. **77**, 103 (1996).
[25] N. Aıchoune, V. Potin, P. Ruterana, A. Hairie, G. Nouet, and E. Paumier, Comp. Mater. Sci. **17**, 380 (2000).
[26] H. K. Cho, J. Y. Lee, G. M. Yang, and C. S. Kim, Appl. Phys. Lett. **79**, 215 (2001).
[27] H. K. Cho, J. Y. Lee, C. S. Kim, G. M. Yang, N. Sharma, and C. Humphreys, J. Cryst. Growth **231**, 466 (2001).
[28] F. C. Massabuau, S.-L. Sahonta, L. Trinh-Xuan, S. Rhode, T. J. Puchtler, M. J. Kappers, C. J. Humphreys, and R. A. Oliver, Appl. Phys. Lett. **101**, 212107 (2012).
[29] A. M. Sanchez, J. A. Gott, H. A. Fonseka, Y. Zhang, H. Liu, and R. Beanland, Nano Lett. **18**, 3081 (2018).
[30] J. Smalc-Koziorowska, C. Bazioti, M. Albrecht, and G. P. Dimitrakopulos, Appl. Phys. Lett. **108**, 051901 (2016).
[31] J. Smalc-Koziorowska, J. Moneta, P. Chatzopoulou, I. G. Vasileiadis, C. Bazioti, Ø. Prytz, I. Belabbas, P. Komninou, and G. P. Dimitrakopulos, Sci. Rep. **10**, 17371 (2020).
[32] P. Vermaut, P. Ruterana, G. Nouet, and H. Morkoç, Philos. Mag. A **75**, 239 (1997).
[33] J. E. Northrup, Appl. Phys. Lett. **72**, 2316 (1998).
[34] P. Ruterana, B. Barbaray, A. Béré, P. Vermaut, A. Hairie, E. Paumier, G. Nouet, A. Salvador, A. Botchkarev, and H. Morkoç, Phys. Rev. B **59**, 15917 (1999).
[35] M. Lee, H. Baik, W. Ryu, Y. Jo, S. Kong, and M. Yang, Nano Lett. **18**, 4866 (2018).
[36] P. Hohenberg and W. Kohn, Phys. Rev. **136**, B864 (1964).
[37] W. Kohn and L. J. Sham, Phys. Rev. **140**, A1133 (1965).
[38] W. Jia, Z. Cao, L. Wang, J. Fu, X. Chi, W. Gao, and L.-W. Wang, Comput. Phys. Commun. **184**, 9 (2013).

[39] W. Jia, J. Fu, Z. Cao, L. Wang, X. Chi, W. Gao, and L.-W. Wang, J. Comput. Phys. **251**, 102 (2013).
[40] D. R. Hamann, Phys. Rev. B **88**, 085117 (2013).
[41] J. P. Perdew, K. Burke, and M. Ernzerhof, Phys. Rev. Lett. **77**, 3865 (1996).
[42] J. Heyd, G. E. Scuseria, and M. Ernzerhof, J. Chem. Phys. **118**, 8207 (2003).
[43] J. Heyd, G. E. Scuseria, and M. Ernzerhof, J. Chem. Phys. **124**, 219906 (2006).
[44] S. Grimme, J. Antony, S. Ehrlich, and H. Krieg, J. Chem. Phys. **132**, 154104 (2010).
[45] See Supplemental Material at http://link.aps.org/supplemental/10.1103/PhysRevB.107.165308 for computational details and additional computational results including the surface terrace edge property of GaN and InN, the kinetic generation process of the SMB, the SMB formation energy in GaN and InN, the lattice parameters for modeling the SMB, the band structures of the SMB in III-nitride materials with larger lattice parameters along the directions perpendicular to the SMB for a benchmark, the band structures of the III-nitride materials without an SMB, the wave function profiles of the SMB, and the spin density profiles of the SMB.
[46] A. F. van Driel, G. Allan, C. Delerue, P. Lodahl, W. L. Vos, and D. Vanmaekelbergh, Phys. Rev. Lett. **95**, 236804 (2005).
[47] H. Zang, X. Sun, K. Jiang, Y. Chen, S. Zhang, J. Ben, Y. Jia, T. Wu, Z. Shi, and D. Li, Adv. Sci. **8**, 2100100 (2021).
[48] S. Adachi, *Optical Constants of Crystalline and Amorphous Semiconductors* (Springer US, Boston, 1999).
[49] Y. Liu, S. Bhowmick, and B. I. Yakobson, Nano Lett. **11**, 3113 (2011).
[50] V. I. Artyukhov, Y. Liu, and B. I. Yakobson, Proc. Natl. Acad. Sci. USA **109**, 15136 (2012).
[51] Z. Zhang, Y. Liu, Y. Yang, and B. I. Yakobson, Nano Lett. **16**, 1398 (2016).
[52] H. Li, L. Geelhaar, H. Riechert, and C. Draxl, Phys. Rev. Lett. **115**, 085503 (2015).
[53] C. Herring, Phys. Rev. **82**, 87 (1951).
[54] M. H. Xie, S. M. Seutter, W. K. Zhu, L. X. Zheng, H. Wu, and S. Y. Tong, Phys. Rev. Lett. **82**, 2749 (1999).
[55] L. X. Zheng, M. H. Xie, S. M. Seutter, S. H. Cheung, and S. Y. Tong, Phys. Rev. Lett. **85**, 2352 (2000).
[56] S. Vézian, J. Massies, F. Semond, N. Grandjean, and P. Vennégués, Phys. Rev. B **61**, 7618 (2000).
[57] M. Xie, L. Zheng, X. Dai, H. Wu, and S. Tong, Surf. Sci. **558**, 195 (2004).
[58] M. H. Xie, M. Gong, E. K. Y. Pang, H. S. Wu, and S. Y. Tong, Phys. Rev. B **74**, 085314 (2006).
[59] I. Bryan, Z. Bryan, S. Mita, A. Rice, J. Tweedie, R. Collazo, and Z. Sitar, J. Cryst. Growth **438**, 81 (2016).
[60] B. M. Shi, M. H. Xie, H. S. Wu, N. Wang, and S. Y. Tong, Appl. Phys. Lett. **89**, 151921 (2006).
[61] C. Li, Y. Wu, T. J. Pennycook, A. R. Lupini, D. N. Leonard, W. Yin, N. Paudel, M. Al-Jassim, Y. Yan, and S. J. Pennycook, Phys. Rev. Lett. **111**, 096403 (2013).
[62] L. Hu, H. Huang, Z. Wang, W. Jiang, X. Ni, Y. Zhou, V. Zielasek, M. G. Lagally, B. Huang, and F. Liu, Phys. Rev. Lett. **121**, 066401 (2018).
[63] J. Kübler, *Theory of Itinerant Electron Magnetism* (Oxford University Press, Oxford, 2017).
[64] T. Cao, Z. Li, and S. G. Louie, Phys. Rev. Lett. **114**, 236602 (2015).
[65] K. Jiang, X. Sun, Z. Shi, H. Zang, J. Ben, H. Deng, and D. Li, Light Sci. Appl. **10**, 69 (2021).
[66] M. Bickermann, B. Epelbaum, and A. Winnacker, J. Cryst. Growth **269**, 432 (2004).
[67] M. Strassburg, J. Senawiratne, N. Dietz, U. Haboeck, A. Hoffmann, V. Noveski, R. Dalmau, R. Schlesser, and Z. Sitar, J. Appl. Phys. **96**, 5870 (2004).
[68] M. Bickermann, B. M. Epelbaum, O. Filip, P. Heimann, S. Nagata, and A. Winnacker, Phys. Status Solidi C **7**, 21 (2010).
[69] R. Collazo, J. Xie, B. E. Gaddy, Z. Bryan, R. Kirste, M. Hoffmann, R. Dalmau, B. Moody, Y. Kumagai, T. Nagashima *et al.*, Appl. Phys. Lett. **100**, 191914 (2012).
[70] T. Ogino and M. Aoki, Jpn. J. Appl. Phys. **19**, 2395 (1980).
[71] D. M. Hofmann, D. Kovalev, G. Steude, B. K. Meyer, A. Hoffmann, L. Eckey, R. Heitz, T. Detchprom, H. Amano, and I. Akasaki, Phys. Rev. B **52**, 16702 (1995).
[72] W. Rieger, R. Dimitrov, D. Brunner, E. Rohrer, O. Ambacher, and M. Stutzmann, Phys. Rev. B **54**, 17596 (1996).
[73] F. A. Ponce, D. P. Bour, W. Götz, and P. J. Wright, Appl. Phys. Lett. **68**, 57 (1996).
[74] E. Calleja, F. J. Sánchez, D. Basak, M. A. Sánchez-García, E. Muñoz, I. Izpura, F. Calle, J. M. G. Tijero, J. L. Sánchez-Rojas, B. Beaumont *et al.*, Phys. Rev. B **55**, 4689 (1997).
[75] U. Kaufmann, M. Kunzer, H. Obloh, M. Maier, C. Manz, A. Ramakrishnan, and B. Santic, Phys. Rev. B **59**, 5561 (1999).
[76] M. A. Reshchikov and H. Morkoç, J. Appl. Phys. **97**, 061301 (2005).
[77] R. Liu, A. Bell, F. A. Ponce, C. Q. Chen, J. W. Yang, and M. A. Khan, Appl. Phys. Lett. **86**, 021908 (2005).
[78] S. Xu, Y. Hao, J. Zhang, T. Jiang, L. Yang, X. Lu, and Z. Lin, Nano Lett. **13**, 3654 (2013).
[79] P. Huang, H. Zong, J. Shi, M. Zhang, X. Jiang, H. Zhong, Y. Ding, Y. He, J. Lu, and X. Hu, ACS Nano **9**, 9276 (2015).